Highly tunable band inversion in AB_2X_4 (A = Ge, Sn, Pb; B = As, Sb, Bi; X = Se, Te) compounds

Lin-Lin Wang *
Ames Laboratory, U.S. Department of Energy, Ames, Iowa 50011, USA

(Received 19 July 2022; accepted 12 September 2022; published 20 September 2022)

Topological materials have been discovered so far largely by searching for existing compounds in crystallographic databases, but there are potentially new topological materials with desirable features that have not been synthesized. One of the desirable features is high tunability resulting from the band inversion with a very small direct band gap, which can be tuned by changes in pressure or strain to induce a topological phase transition. Using density-functional theory (DFT) calculations, we have studied the septuple layered AB_2X_4 series compounds, where A = (Ge, Sn and Pb), B = (As, Sb and Bi), and X = (Se and Te). With the DFT thermodynamic stability validated by the already-reported compounds in these series, we predict stable Se compounds, which are not found in crystallographic database. Among them, we find that $GeBi_2Se_4$ and $GeSb_2Se_4$ having a small direct band gap at the Z point are very close to a strong topological insulator, which can be tuned by a moderate pressure to induce the band inversion. Importantly, the topological features with the small direct band gap are well isolated in both momentum and energy windows, which offers high tunability for studying the topological phase transition.

DOI: 10.1103/PhysRevMaterials.6.094201

I. INTRODUCTION

Symmetry-protected topological states [1–4] have greatly expanded our understanding of electronic band structures in condensed-matter physics and materials science. With the development of new understanding in band-structure topology from symmetry-based indicators and the related approaches [5–11], symmetry-protected topological features have been classified and topological materials have been tabulated in databases. Several groups have compiled catalogs [12–15] of topological materials by searching crystallographic databases among existing compounds, calculating band structures and topological index. However, there are potentially new topologically nontrivial compounds that have not been synthesized or in crystallographic databases. Even more interesting is that such new compounds may bring new tunability and push the limits in topological features. One such limit is to find a topological insulator (TI) with a band gap larger than Bi_2Se_3. But, the other limit of a very small direct band gap is also interesting for the purpose of high tunability to induce topological phase transitions. $ZrTe_5$ is a good example sitting near the phase boundary [16,17] between a strong and weak TI with a critical Dirac point [18] in between, which can be tuned by pressure, strain, temperature, and phonons. Weyl points and many other interesting properties [19,20] can also be induced in $ZrTe_5$. Thus, it is desirable to find more compounds sitting near the topological phase boundary to a normal insulator or another topological phase with the key features isolated in both energy and momentum windows for versatile control and manipulation.

One way to search for new topological materials is to look into the underexplored area in phase diagrams and combinations of elements. For the septuple-layered AB_2X_4 series, where A = (Ge, Sn, and Pb) for group IV, B = (As, Sb, and Bi) for group V, and X = (Se, Te) for group VI elements, the Te compounds are well explored, while Se ones are not. Eremeev *et al.* [21] have studied several 1-2-4 compounds and found most are strong TIs (STIs). For example, $PbBi_2Te_4$ has been reported [22] from angular-resolved photoelectron spectroscopy (ARPES) as an STI with a band inversion at the Z point of the Brillouin-zone (BZ) boundary, in contrast to that at the Γ point of the BZ center in the Bi_2Te_3 series. More recently the magnetic version in this structure-type $MnBi_2Te_4$ series [23–29] has been discovered to be an intrinsic antiferromagnetic TI with the few layers hosting quantum anomalous Hall and axion insulator behaviors [30,31]. In contrast, the Se compounds have been much less studied. Only very recently, $MnBi_2Se_4$ thin films [32] have been grown in molecular-beam epitaxy. Se-Te alloyed septuple-layered compounds have also been recently synthesized [33].

In this paper, using density-functional theory (DFT) calculations with different exchange-correlation (XC) functionals, we systematically calculate the thermodynamic stability, electronic band structure, and topological properties of both Te and Se compounds in AB_2X_4 series. Out of nine different cation combinations for Te compounds in this structure, seven have been reported, except for $SnAs_2Te_4$ and $PbAs_2Te_4$, which we find are thermodynamically unstable with decomposition into two binary compounds in our DFT calculations, agreeing with experimental observations. In contrast, the only Se compounds that have been reported [34,35] are $SnBi_2Se_4$ and $PbBi_2Se_4$, with the latter being an alloy. Using these reported compounds to establish the predictability of the DFT calculations for phase stability, we find that eight of nine

*llw@ameslab.gov

Se compounds are thermodynamically stable with respect to the decomposition into the binary compounds. Although with the modified Becke-Johnson [36] (mBJ) exchange potential to correct band gap the band inversion in Se compounds is lifted, we find that two stable Se compounds, $GeBi_2Se_4$ and $GeSb_2Se_4$, are very close to an STI with a small direct band gap at the Z point. We predict that a moderate hydrostatic pressure can induce the topological phase transition with the band inversion and a critical Dirac point at the Z point, such as 1.7 GPa for $GeBi_2Se_4$. More importantly, these topological features are well isolated in both momentum and energy windows, which offers high tunability and clean Fermi surface for studying the topological phase transition.

II. COMPUTATIONAL METHODS

All DFT [37,38] calculations with spin-orbit coupling (SOC) have been performed with different XC functionals using a plane-wave basis set and projector augmented-wave method, as implemented in the Vienna *Ab initio* Simulation Package [39,40] (VASP). Besides PBEsol [41], for van der Waals (vdW) interaction we have considered vdW density functional (vdW-DF) of optB86b [42]. We have also used the semiempirical vdW parameter sets of D2 [43], D3 [44], and D3 with Becke-Johnson damping [45] (or D3BJ). We use a kinetic energy cutoff of 300 eV, Γ-centered Monkhorst-Pack [46] ($12 \times 12 \times 4$) k-point mesh, and a Gaussian smearing of 0.05 eV. The ionic positions and unit-cell vectors are fully relaxed with the remaining absolute force on each atom less than $0.02\,\mathrm{eV/Å}$. For a few cases with available experimental lattice parameters, ionic relaxation only has also been considered for comparison to the results from full relaxation. Using maximally localized Wannier functions [47,48], tight-binding models have been constructed to reproduce closely the band structure including SOC within 1 eV of the Fermi level by using group IV sp, group V- and VI p orbitals. The surface spectral functions have been calculated with the surface Green function methods [49,50] as implemented in WANNIERTOOLS [51].

III. RESULTS AND DISCUSSION

A. Structural-energy prediction

AB_2X_4 in the rhombohedral $GeAs_2Te_4$-type (Pearson symbol $hR21$) crystal structure of space group 166 ($R\bar{3}m$) and its first Brillouin zone are shown in Fig. 1(a), where $A =$ (Ge, Sn, and Pb), $B =$ (As, Sb, and Bi), and $X =$ (Se and Te), respectively. It has septuple-layered units in the ab plane coupled weakly via vdW interaction along the (001) direction. Within each septuple unit, the stacking is X-B-X-A-X-B-X, where A (group IV element) occupies the central, and $B-$ (group V) and X (group VI) elements occupy the three outmost atomic layers. The two group VI sites are not equivalent. Groups IV, V, and VI elements have the nominal valence charge of $+2$, $+3$, and -2, respectively. Such structure belongs to a large group of rhombohedral and hexagonal vdW layered materials with charge balance for being narrow-gap semiconductors, thermoelectrics, and TIs.

The DFT-calculated formation energy (E_f) in eV per formula unit (eV/f.u.) are plotted for AB_2X_4 with respect to binary AX and B_2X_3 compounds in Figs. 1(b)–1(f) for different XC functionals with SOC. The ground-state crystal structures of the binary AX and B_2X_3 compounds are listed in Table I. These binary compounds are also fully relaxed with the corresponding XC functionals for the E_f calculation. Considering the deviation of DFT-calculated E_f vs experimental values due to the limitation of XC functional, there is likely a shift of energy zero [52]. For example, in Fig. 1(d) with D3+SOC, $GeBi_2Te_4$ has $E_f = 0.05\,\mathrm{eV/f.u.}$, but it was found stable in experiment. When the effective energy zero is shifted to that of $GeBi_2Te_4$, we find seven out of nine Te compounds are stable, except for $PbAs_2Te_4$ and $SnAs_2Te_4$, which is in a good agreement with experimental observations. The results from the five different XC functionals in Fig. 1 all agree that $PbAs_2Te_4$ and $SnAs_2Te_4$ are the two unstable ones among the nine Te compounds. Using the criteria that the rest of the seven Te compounds are thermodynamically stable as found in experiment, an energy shift of about $E_f = 0.05\,\mathrm{eV/f.u.}$ is needed for all five XC functionals. The almost-same size of the energy zero shift indicates a systematic error in PBE-based XC functionals for these compounds.

TABLE I. Binary AX and B_2X_3 compounds in their ground-state crystal structure as listed in the sequence of Pearson symbol, space group, and structural type.

AX	Ge	Sn	Pb
Se	$oP8$, 62, GeS	$oP8$, 62, GeS	$cF8$, 225, NaCl
Te	$hR6$, 160, GeTe	$cF8$, 225, NaCl	$cF8$, 225, NaCl
B_2X_3	As	Sb	Bi
Se	$mP20$, 14, As_2S_3	$oP20$, 62, Sb_2Se_3	$hR15$, 166, Bi_2Te_3
Te	$hR15$, 166, Bi_2Te_3	$hR15$, 166, Bi_2Te_3	$hR15$, 166, Bi_2Te_3

With the energy zero established, the results for Se compounds can be separated into two groups. PBEsol and D3BJ give similar results to each other that all Se compounds are stable, while D2, D3, and optB86b give all are stable except for $PbAs_2Se_4$. The change of E_f across the series is also similar for PBEsol and D3BJ, but different from the other three XC functionals. The difference among the two groups of XC functionals also reflects in the optimized lattice constants and band gaps as we will discuss later. From Fig. 1, the overall trend is that Se compounds on average are more stable than the corresponding Te ones with respect to the decomposition into binaries, except for some Se compounds with D2. Another important trend for Te compounds is that, except for Ge series, the stability increases with group V element going from As to Sb to Bi. This trend is also largely true for the Se compounds with D2, D3, and optB86b. Interestingly, we find that eight out of nine Se compounds are thermodynamically stable with respect to binary compounds, except for $PbAs_2Se_4$, as determined by most XC functionals used.

The good predictability of DFT can also be seen in the optimized lattice constants. The direct comparison between the DFT-optimized lattice constants a_{DFT} and the nine available experimental a_{expt} with the five XC functionals are plotted in Figs. 2(a)–2(e) and c_{DFT} vs c_{expt} in Figs. 2(f)–2(j), respectively. Again, PBEsol and D3BJ give very similar

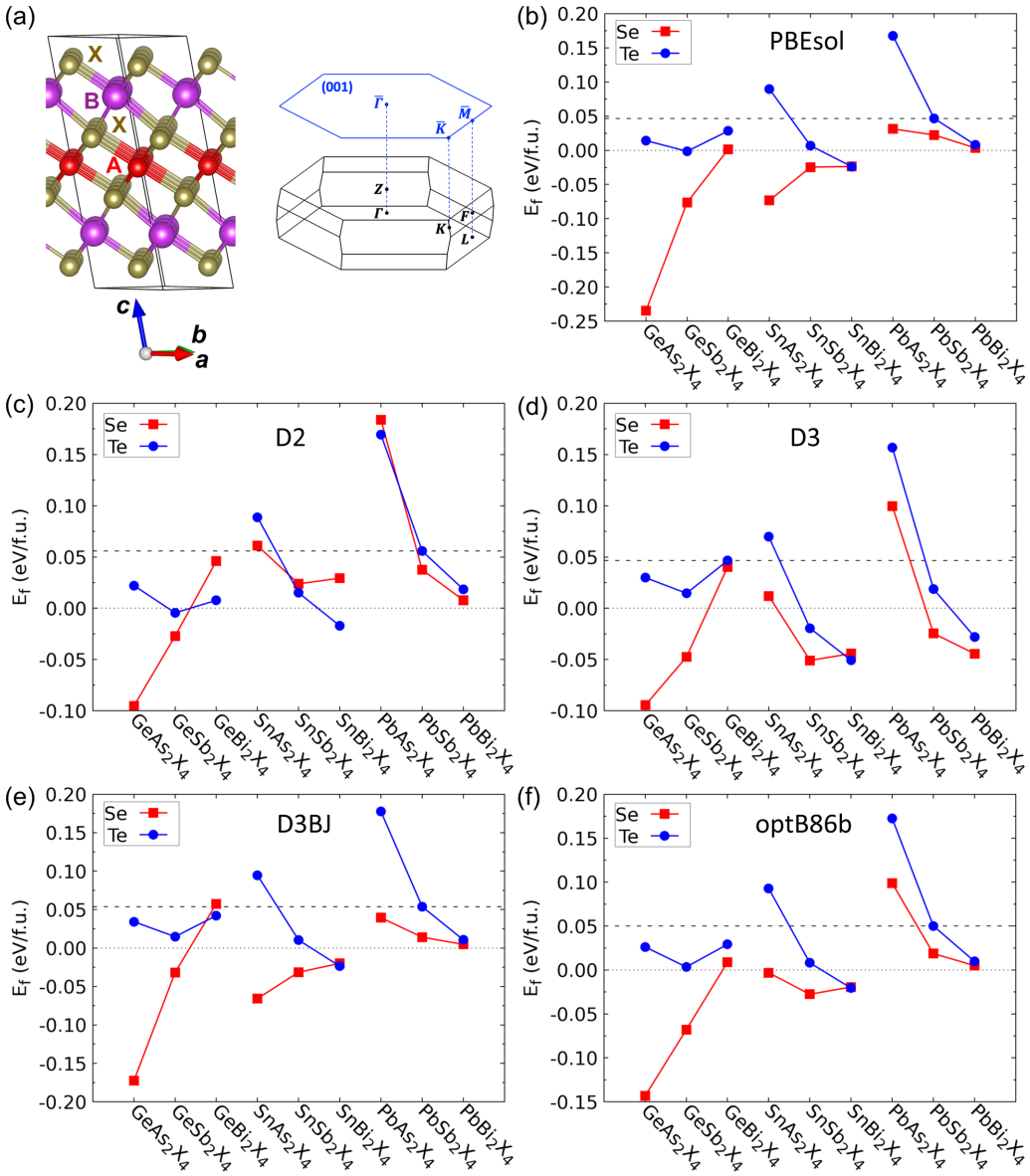

FIG. 1. (a) Crystal structure and Brillouin zone (BZ) of AB_2X_4 in the rhombohedral $GeAs_2Te_4$-type ($hR21$) of space group 166 ($R\bar{3}m$). $A =$ (Ge, Sn, and Pb) are in red, $B =$ (As, Sb, and Bi) in purple, and $X =$ (Se and Te) in brown spheres. High-symmetry k points and those on (001) surface BZ are labeled. (b)–(f) DFT-calculated formation energy (E_f) with different XC functional with SOC in eV per formula unit (f.u.) of AB_2X_4 with respect to binary AX and B_2X_3 compounds. The dotted and dashed lines are for energy zero and that shifted to $GeBi_2Te_4$ or $PbSb_2Te_4$ as found stable in experiment, respectively.

results of more accurate a, but c is largely underestimated. While both D3 and optB86b overestimate a by a similar amount, the latter give better prediction in c. Lastly, D2 slightly underestimates a; the c prediction is as good as optB86b. These differences are also directly reflected in the mean absolute error (MAE) and root-mean-squared error (RMSE) as listed in Table II. While PBEsol and D3BJ have the smallest MAE and RMSE for a, those for c are the largest. Even for D3+SOC, it slightly overestimates a, while underestimates c, but they are both within +/–2%, the acceptable range for DFT predictability. The experimental data are mostly for Te compounds. Notably, the Se data (red dot) for $SnBi_2Se_4$ and $PbBi_2Se_4$ are in line with the Te compounds, as well as the alloyed structures (open symbols). Together with the thermodynamic stability in Fig. 1, these comparisons to experimental data show the reliable predictability of DFT for structural energy of these layered compounds. There are

TABLE II. MAE and RMSE for the fully relaxed nine compounds with different XC functionals in Fig. 2. Numbers in bold highlight the minimum MAE and RMSE.

MAE/RMSE (Å)	a	c
FR-PBEsol	**0.014/0.017**	0.826/0.923
FR-D2	0.027/0.030	0.450/0.495
FR-D3	0.055/0.059	0.606/0.694
FR-D3BJ	0.018/0.020	0.821/0.935
FR-optB86b	0.043/0.046	**0.378/0.490**

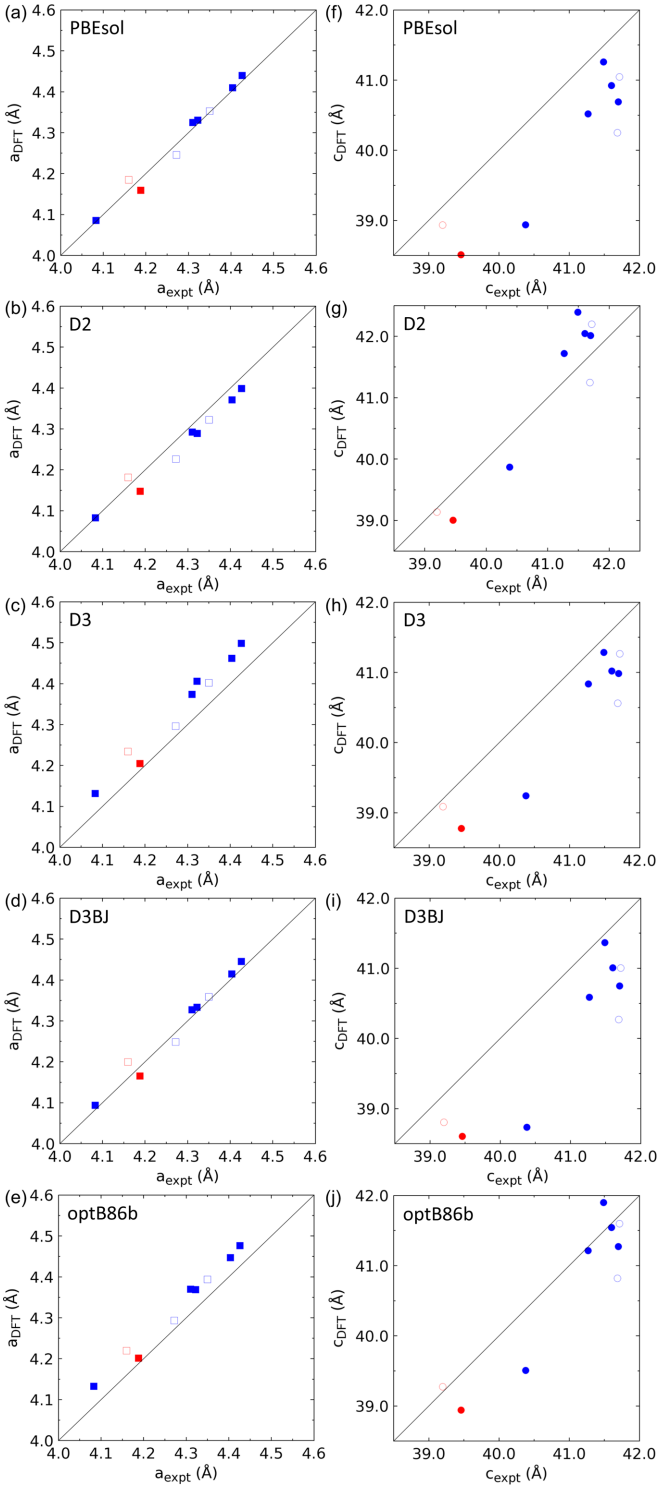

FIG. 2. Comparison of the DFT-optimized lattice constants with experimental data for (a)–(e) a and (f)–(j) c using different XC functionals for nine AB_2X_4. The blue and red are for AB_2Te_4 and AB_2Se_4, respectively. The open symbols are reported alloys for $GeSb_2Te_4$, $PbSb_2Te_4$, and $PbBi_2Se_4$.

some differences among the five XC functionals. Noticeably, in contrast to D2, D3 with geometry-dependent dispersion coefficients and r^{-8} besides r^{-6} terms give results very close to the vdW-DF XC functional optB86b. Then, interestingly, instead of the zero-damping, D3BJ for D3 with the BJ damping gives very similar results to PEBsol for these compounds.

TABLE III. Band gaps of the four compounds with experimental data compared to the calculated results with IR in experimental lattice constants and FR structures using different XC functionals without and with mBJ exchange potential. The numbers in italics indicate trivial band gap, while the others are with band inversion for STI.

Δ (eV)	$GeSb_2Te_4$	$GeBi_2Te_4$	$SnSb_2Te_4$	$PbBi_2Te_4$
Experiment	0.1	0.12, 0.2	0.2	0.23
IR-PBEsol/mBJ	*0.07/0.14*	0.08/0.06	0.14/0.09	0.12/0.15
IR-D2/mBJ	*0.06/0.13*	0.06/0.04	0.10/0.02	0.13/0.13
IR-D3/mBJ	*0.02/0.09*	0.09/0.07	0.16/0.12	0.12/0.16
IR-D3BJ/mBJ	*0.00/0.07*	0.07/0.07	0.16/0.12	0.12/0.15
IR-optB86b/mBJ	0.02/*0.02*	0.09/0.07	0.18/0.13	0.12/0.16
FR-PBEsol/mBJ	0.08/0.03	0.09/0.06	0.09/0.16	0.10/0.13
FR-D2/mBJ	0.05/0.02	0.07/0.03	0.07/0.00	0.13/0.15
FR-D3/mBJ	0.11/0.07	0.10/0.07	0.14/0.13	0.12/0.12
FR-D3BJ/mBJ	0.07/0.03	0.07/0.06	0.10/0.16	0.12/0.15
FR-optB86b/mBJ	0.09/0.07	0.07/0.08	0.13/0.13	0.13/0.14

B. Band-gap prediction

After establishing the reliable predictability of DFT structural energy for AB_2X_4, we next discuss the predicted band gap, band structure, and topological properties. The combination of vdW-DF XC functional and mBJ exchange potential has been shown to give good results to band gaps for vdW materials [53,54] with the latter being a meta-GGA to add orbital-dependent correction using the converged Kohn-Sham wave functions of the vdW-DF optimized crystal structures. Here, we will also combine mBJ with PBEsol XC functional to calculate the band structures, as well as other semiempirical vdW energy corrections with the correspondingly optimized crystal structures. Among the 18 compounds, four Te compounds, $GeSb_2Te_4$, $GeBi_2Te_4$, $SnSb_2Te_4$, and $PbBi_2Te_4$, have their band gap measured experimentally and were determined as STI by ARPES. For these compounds, because of the available experimental lattice constants, we will also calculate band structures with only ionic relaxations (IR), besides the full relaxation (FR) in different XC functionals without and with mBJ exchange potential. These different band-gap results are listed in Table III for comparison and also plotted in Figs. 3(a) and 3(b) for IR and FR, respectively. The open symbols are for the results with mBJ correction.

As listed in Table III, for $GeSb_2Te_4$, a p-doped STI with a small band gap of 0.1 eV as determined [55] by ARPES, IR structures give a trivial narrow-gap semiconductor with a band gap from 0.00 to 0.07 eV, except for optB86b giving it as an STI with a gap of 0.02 eV. With mBJ, the band gap for the trivial narrow-gap semiconductor increases by 0.07 eV. The band inversion for STI is removed in optB86b with mBJ, although the resulting band-gap size is also 0.02 eV. All five XC functionals in IR with mBJ give $GeSb_2Te_4$ as trivial. In a distinct contrast, all five XC functionals with FR structures give it as a STI agreeing with experiment and the calculated band gap ranges from 0.05 to 0.11 eV. With mBJ,

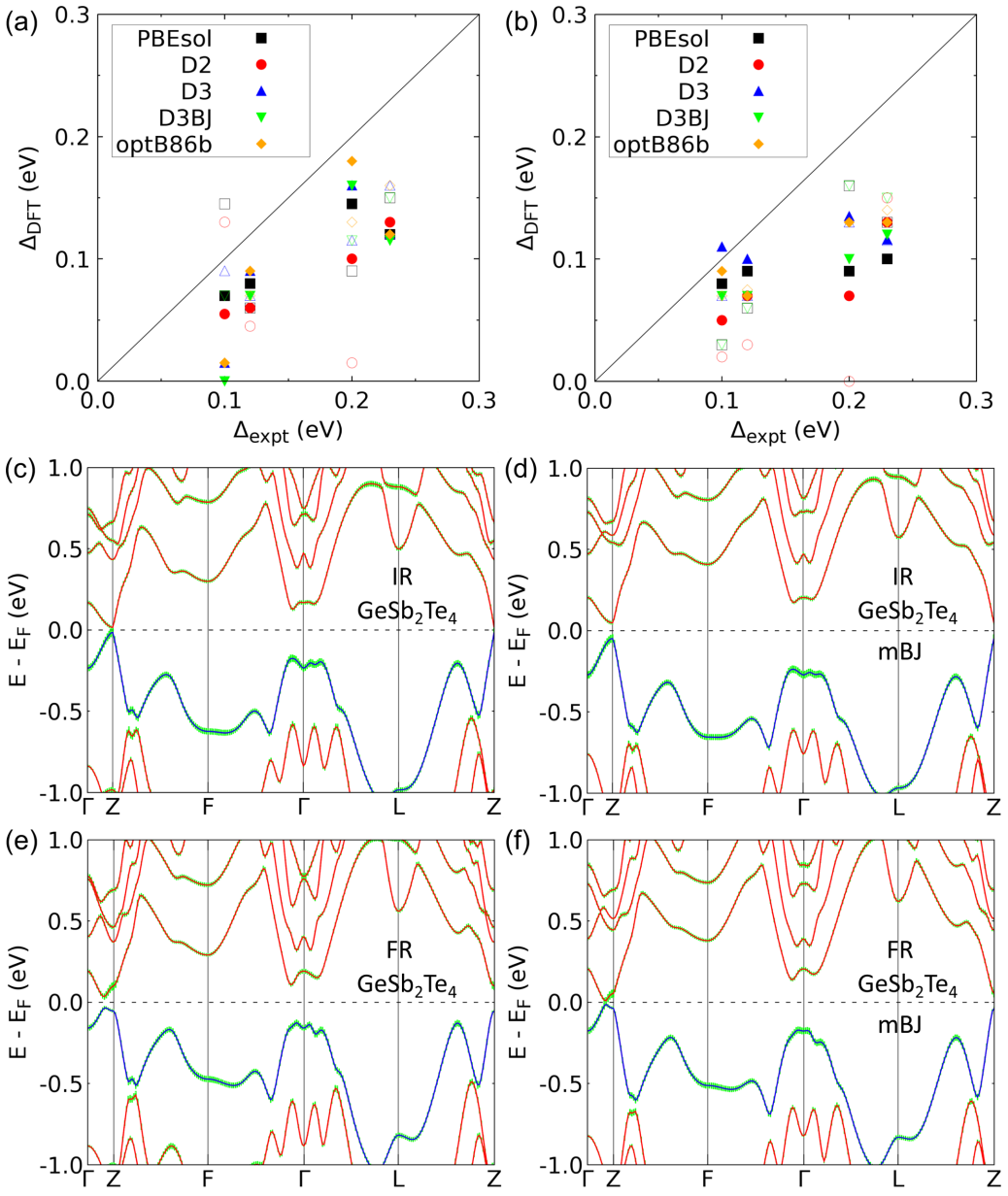

FIG. 3. Comparison between the four available experimental band gaps (Δ_{expt}) and the calculated ones (Δ_{DFT}) using (a) ionically relaxed (IR) structures with experimental lattice constants and (b) fully relaxed (FR) with DFT-optimized lattice constants. The open symbols are mBJ results for the corresponding XC functionals. Band structure of $GeSb_2Te_4$ calculated using D3+SOC with (c) IR structure and (d) also mBJ. Those with (e) FR and (f) also mBJ. The top-valence band is in blue and the green shadow stands for the projection on Te p orbitals of the outmost layer. The high-symmetry k points are in Fig. 1(a).

the band gap for FR structures all decreases, but it remains as an STI for all five XC functionals. These opposite changes for $GeSb_2Te_4$ in IR and FR without and with mBJ can be seen as the opposite relative positions of the open and filled symbols at $\Delta_{expt} = 0.1$ eV for $GeSb_2Te_4$ in Figs. 3(a) and 3(b), respectively. These differences are showcased by the bulk band structures calculated with D3+SOC in Figs. 3(c)–3(f) for $GeSb_2Te_4$, for which the BZ and high-symmetry k points are shown in Fig. 1(a). The band inversion in these compounds happens near the E_f at the Z point. As shown in Fig. 3(c) for IR, the small gap of 0.02 eV is a direct one without band inversion at the Z point. With mBJ in Fig. 3(d), the trivial direct gap is enlarged to 0.09 eV, as the lowest conduction band at the F point is pushed to higher energy and the highest valence band along L-Z is pushed to lower energy, which are expected with mBJ. In contrast, for FR in Fig. 3(e), the band gap of 0.11 eV near the Z point is inverted, clearly shown by the green shade projected on the outmost Te p orbitals. With mBJ, the lowest conduction band at the F point is still pushed higher and the highest valence band along L-Z is pushed lower in energy aiming to increase the band gap. But, because of the band inversion, the tendency of mBJ to separate valence- and conduction band needs to first reduce the band-inversion region, but not necessarily the band gap itself. As seen in Fig. 3(f) when compared to 3(e), the size of the band-inversion region around the Z point becomes smaller with mBJ, but

TABLE IV. MAE and RMSE for the four compounds with experimental data compared to the calculated results with structures from the ionic relaxation in experimental lattice constants and full relaxation using the different XC functionals and also mBJ as plotted in Fig. 3. Numbers in bold highlight the minimum MAE and RMSE.

MAE/RMSE (eV)	IR	FR
PBEsol	0.059/0.066	0.072/0.087
PBEsol-mBJ	0.074/0.078	0.068/0.071
D2	0.076/0.080	0.082/0.089
D2-mBJ	0.098/0.113	0.112/0.123
D3	0.066/0.074	**0.052**/0.066
D3-mBJ	**0.054/0.061**	0.066/0.073
D3BJ	0.076/0.083	0.072/0.080
D3BJ-mBJ	0.061/0.065	0.062/0.064
optB86b	0.061/0.072	0.058/0.066
optB86b-mBJ	0.069/0.070	0.059/**0.063**

as the band inversion is not lifted, the band gap between the inverted bands actually decreases, changing from 0.11 to 0.07 eV. Thus, the correction with mBJ can either increase or decrease the band-gap size, depending on the presence of band inversion or not, as well as if the gap is a direct or indirect one.

For the other three experimentally measured Te compounds as STI, $GeBi_2Te_4$ was confirmed [56] to have a surface Dirac point by ARPES with a bulk band gap of 0.2 eV. A later ARPES study [57] put the bulk band gap at 0.12 eV. $SnSb_2Te_4$ is a heavily *p*-doped STI the ARPES study estimated [58] the bulk gap to be a minimum of 0.2 eV. Our calculated band gap agrees with the previous PBEsol calculation [59] of 0.12 eV. For $PbBi_2Te_4$, it has been measured [22] by ARPES as an STI with a band gap of 0.23 eV. Our calculated band gap also agrees with the previous calculation [22], giving an underestimated band gap around 0.12 eV. From the MAE and RMSE compiled in Table IV that are based on the limited data

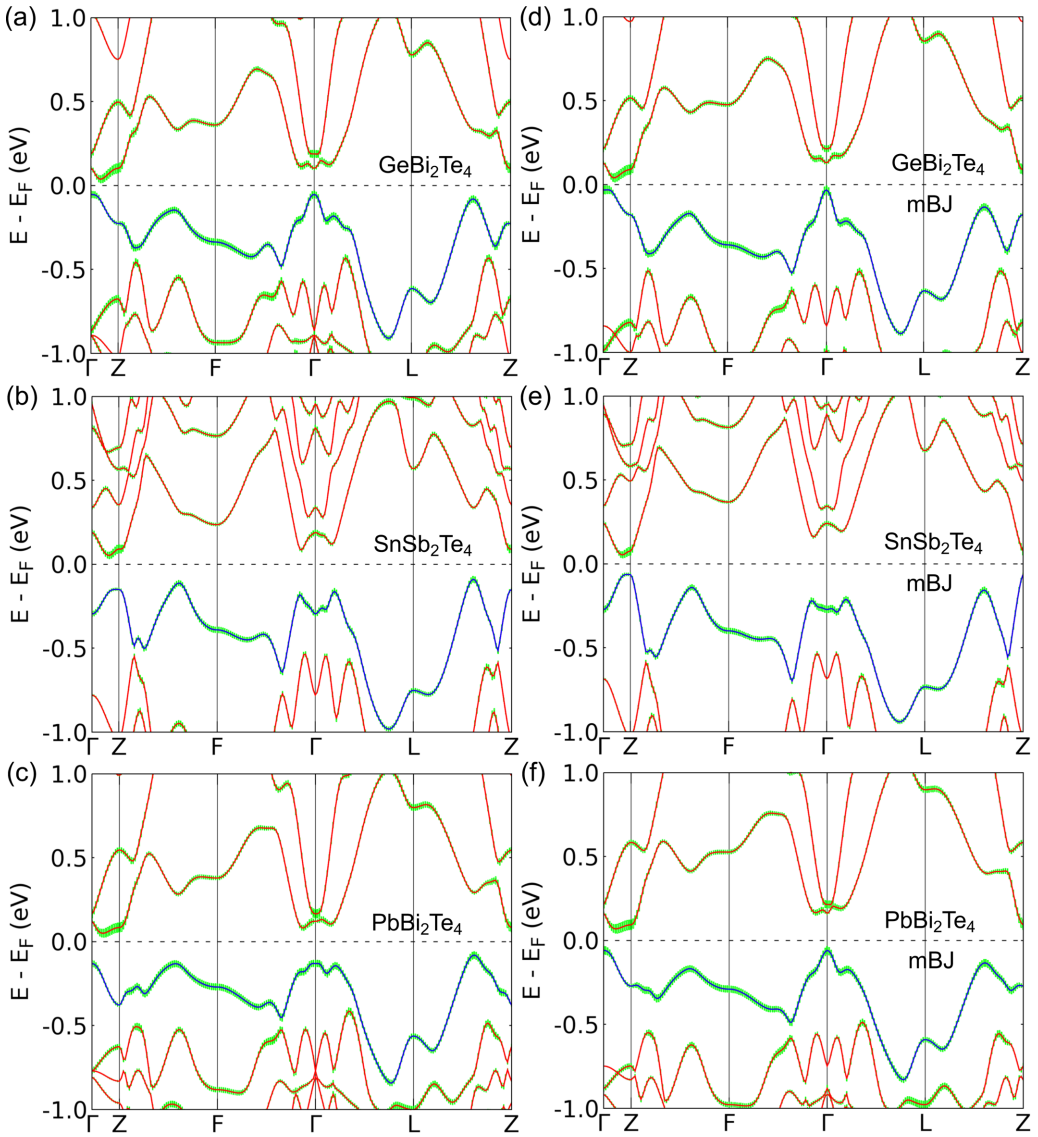

FIG. 4. (a)–(c) Band structure calculated in D3+SOC with the fully relaxed crystal structures for $GeBi_2Te_4$, $SnSb_2Te_4$, and $PbBi_2Te_4$, respectively. (d)–(f) Corresponding band structures with mBJ. The top-valence band is in blue and the green shadow stands for the projection on Te *p* orbitals of the outmost layer.

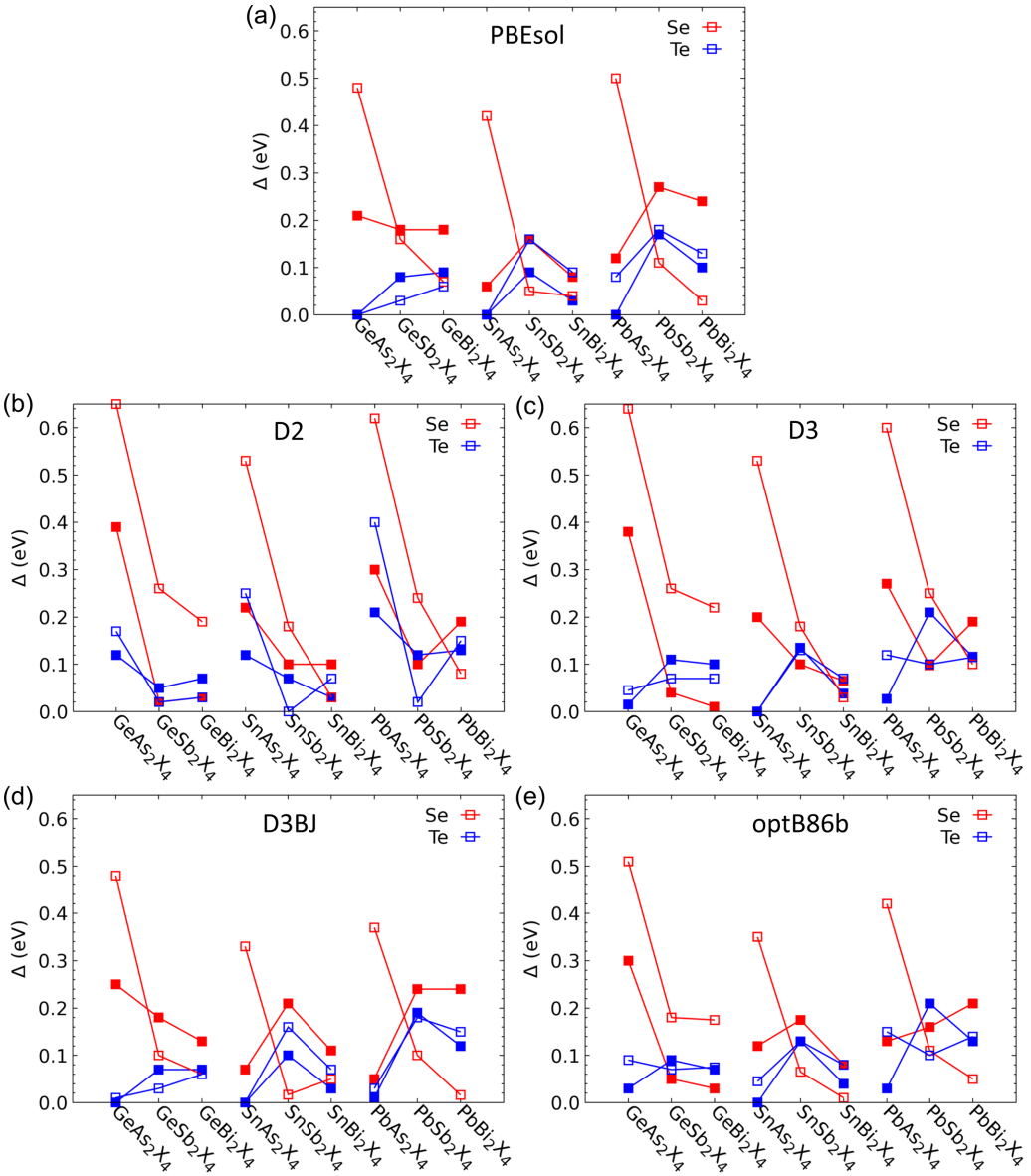

FIG. 5. DFT-calculated band gap (Δ) for AB_2X_4. The blue and red are for AB_2Te_4 and AB_2Se_4, respectively. The solid and open symbols are for the different XC functionals and the corresponding mBJ results, respectively.

of the four Te compounds, the D3 emerges as the choice of XC functional for band-structure calculation. D3 has the smallest MAE and its RMSE is also not far from the smallest. Thus, for topological band structures that will be discussed below, D3 will be used. The D3+SOC band structures with FR of the other three known STI Te compounds are plotted in Fig. 4. It clearly shows that the band-inversion region for the Bi compounds is larger than the Sb one due to the stronger SOC. The band-inversion region is also reduced when using mBJ. The band gap can increase or decrease depending on if it is a direct gap near the Z point like $GeSb_2Te_4$ or indirect gap like these three compounds. But, for all the four Te compounds, the FR structures with five different XC functionals predict they are all STI, agreeing with experiment.

Ideally, more experimental data from Se compounds are needed to more effectively validate the DFT prediction of band gap. From the MAE and RMSE in Table IV, PBEsol and D3BJ give good lattice constant of a, but the calculated band gap for FR structures are not as close to experiments as the other group of XC functionals, mostly due to the inaccurate prediction on c, which is also important for the band inversion at the Z point. Although IR with experimental lattice constants for band-structure calculation has been regarded as reliable most of time, here it misses the band inversion in $GeSb_2Te_4$. This shows the sensitivity of band inversion and band gap to the change of lattice constants besides the ionic coordinates, which makes pressure an effective knob to tune topological phase transition in these compounds.

The calculated band gaps for all the compounds with different XC functionals are plotted in Fig. 5. These results are with FR structures without and with mBJ potential to correct the band gap. The Te compounds mostly have an indirect gap, while the Se ones mostly have a direct band gap at the Z point. As shown in Fig. 5, across the different compounds,

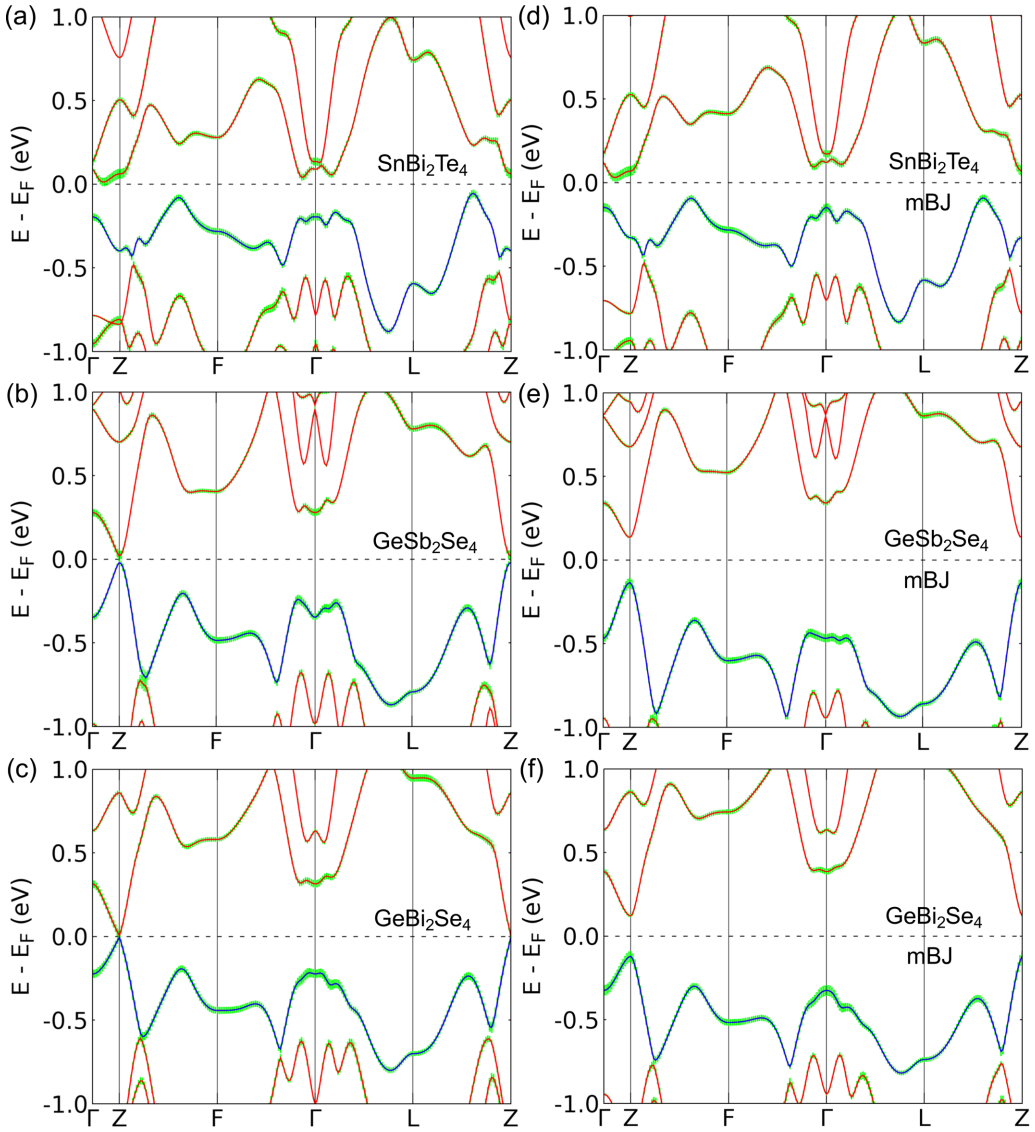

FIG. 6. (a)–(c) Band structure calculated in D3+SOC with the fully relaxed crystal structures for $SnBi_2Te_4$, $GeSb_2Se_4$, and $GeBi_2Se_4$, respectively. (d)–(f) Corresponding band structures with mBJ. The top-valence band is in blue and the green shadow stands for the projection on X p orbitals of the outmost layer.

the results from D3BJ are quite similar to those from PBEsol, following the same kind of similarity in the predicted lattice constants and formation energy. For Te compounds, except for D2, the mBJ band gaps are very close to the one without such correction. For Se compounds, the ones with As have the largest band gap predicted with mBJ, because they are normal semiconductors without band inversion. When there is a band inversion, the mBJ needs to first overcome the band inversion before enlarge the band gap. So, for compounds with band inversion, mBJ does not necessarily increase the band gap much. In contrast for trivial systems without band inversion, mBJ can open up a significantly larger band gap, which are mostly As compounds.

C. Topological tunability

For topological classification of the band structures of AB_2X_4, due to the inversion symmetry, the Fu-Kane [60] type Z_2 topological index based on parity eigenvalues can be calculated. The septuple structure is known for the band inversion at the Z point with the Fu-Kane topological index of (1;111), in contrast to the band inversion at the Γ point in the quintuple-layered Bi_2Te_3 type. The band inversion is between group VI p_z and group V p_x and p_y orbitals. From our calculations, most Te compounds with Sb and Bi are STI, while most As ones are not, except for $SnAs_2Te_4$, but it is not thermodynamically stable. These results show the importance of SOC for band inversion, because As is the lightest in group V. Without mBJ correction, most Se compounds except for the ones with As are calculated as STI and some have sizable band gap and some have a very small gap. With mBJ correction, all Se compounds calculated in D2, D3, and optB86b become topologically trivial semiconductors, but importantly these band gaps are quite small, which can be tuned by pressure.

For example, we predict two thermodynamically stable Se compounds, $GeBi_2Se_4$ and $GeSb_2Se_4$, not found in

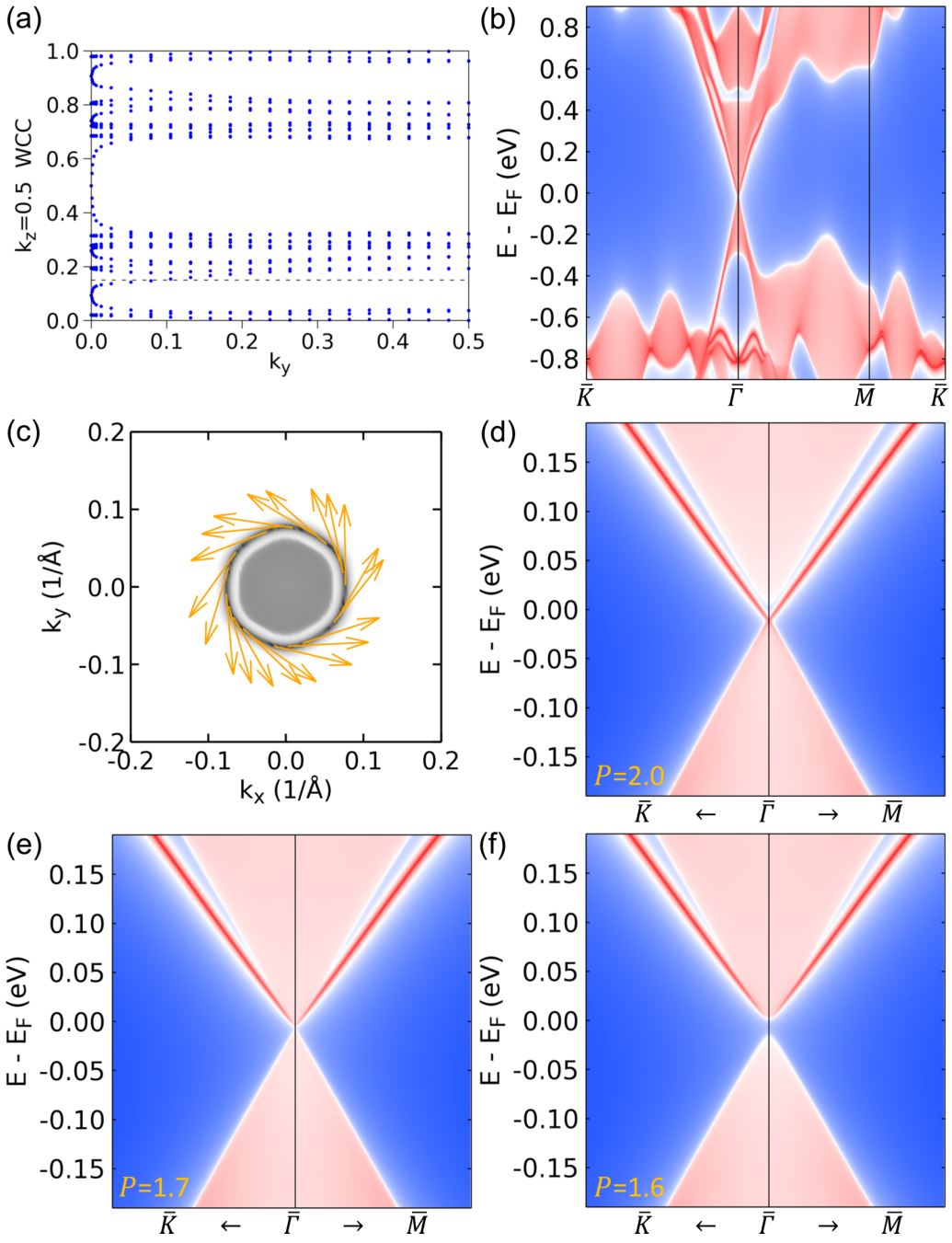

FIG. 7. (a) Wannier charge center (WCC) evolution on $k_z = 0.5$ plane, (b) (001) surface spectral function and (c) spin texture on 2D Fermi surface at $E_F + 0.2$ eV for $GeBi_2Se_4$ with the hydrostatic pressure (P) of 2.0 GPa, showing the nontrivial topology of an STI with $Z_2 = (1; 111)$. The high-symmetry k points are in Fig. 1(a). The surface spectral function zoomed around $\bar{\Gamma}$ point with P of (d) 2.0, (e) 1.7, and (f) 1.6 GPa, calculated with mBJ+SOC. The $P = 1.7$ GPa gives a critical bulk Dirac point.

crystallographic database, are narrow-gap semiconductors based on mBJ, but close to the topological phase transition to STI. Without mBJ, $GeBi_2Se_4$ and $GeSb_2Se_4$ are STI having a very small direct band gaps of 0.01 and 0.04 eV, and the bulk band structures are shown in Figs. 6(b) and 6(c), respectively. With mBJ, the band inversion is lifted and the gap is increased to 0.22 and 0.26 eV [Fig. 6(e) and 6(f)]. Unlike most Te compounds having an indirect band gap, such as $SnBi_2Te_4$ in Figs. 6(a) and 6(d), the band gap for these Se compounds is direct at the Z point. Away from the Z point, the top-valence and bottom-conduction bands are well separated [Figs. 6(e) and 6(f)]; thus, these two Se compounds have their tunable band-inversion region isolated in both momentum and energy windows, which is a desirable feature for experimental detection and control of the topological properties. For these Se compounds, especially $GeBi_2Se_4$, the small band gap means it is very close to the critical point of topological phase transition between an STI and normal insulator with a critical Dirac point at the Z point, which can be tuned by pressure, strain, phonon, and temperature. Previously $ZrTe_5$ has been a

prototype of such highly tunable topological material. Here, we predict that $GeBi_2Se_4$ and $GeSb_2Se_4$ are also materials with high tunability in band-structure topology. The sensitivity of the band dispersion to pressure here is similar to that in $AECd_2As_2$ series [61] for inducing a Dirac point.

To demonstrate the high tunability of these narrow-gap semiconductors that are close to STI, the surface spectral functions of $GeBi_2Se_4$ (001) have been calculated with different hydrostatic pressure (P) up to 2.0 GPa as shown in Fig. 7. First, the Wannier charge center (WCC) evolution on the $k_z = 0.5$ plane in Fig. 7(a) shows the nontrivial band topology for $GeBi_2Se_4$ under 2.0 GPa with the band inversion at the Z point. As plotted in Fig. 7(b), the spectral function has topological surface states enveloping the bulk conduction bands [see Fig. 1(a) for the hexagonal surface BZ] and converging toward the $\bar{\Gamma}$ point, which is well isolated in both momentum and energy windows. Figure 7(c) shows the in-plane spin texture from the upper surface Dirac cone enveloping the bulk conduction bands at energy as high as $E_F + 0.2$ eV. Because the band inversion is only at the Z point, when projected on (001), the nontrivial surface Dirac point is expected to appear at the $\bar{\Gamma}$ point. After zoomed-in Fig. 7(d), indeed there is only one surface Dirac point at the $\bar{\Gamma}$ point with a small bulk band gap. With smaller pressure, the band gap is first closed in Fig. 7(e) and then reopened in Fig. 7(f) showing a topological phase transition. Less than $P = 1.6$ GPa as in Fig. 7(f), the band inversion is not present, which is confirmed by the surface states only attaching to the bulk conduction bands for a normal insulator. Importantly, at $P = 1.7$ GPa in Fig. 7(e), a critical bulk Dirac point emerges at the Z point with both the surface states and Dirac point projection converging at the $\bar{\Gamma}$ point. Thus, we propose that the high tunability of the topological phase transition in $GeBi_2Se_4$ and $GeSb_2Se_4$ can potentially be explored with pressure, strain, and coherent phonons as found in pump-probe experiments for $ZrTe_5$. We also emphasize the need to have experimentally measured band gaps for Se compounds to validate the different DFT-calculated results.

IV. CONCLUSION

In conclusion, using density-functional theory calculations, we have studied the septuple-layered AB_2X_4 series compounds with $A =$ (Ge, Sn, and Pb), $B =$ (As, Sb, and Bi), and $X =$ (Se and Te). Unlike the seven Te compounds, only two Se compounds have been reported in these series. Using these reported compounds to validate the thermodynamic stability from DFT calculations with different exchange-correlation functionals, we predict stable Se compounds that are not found in crystallographic database. Interestingly, we find $GeBi_2Se_4$ and $GeSb_2Se_4$ with a small direct band gap are close to a topological phase transition to strong topological insulators with a band inversion at the Z point, which can be induced by a moderate hydrostatic pressure. Additionally, the topological features with the small direct band gap in these compounds are well isolated in both momentum and energy windows, which offers high tunability for studying the topological phase transition. Using $GeBi_2Se_4$ as the example, we show that under a small hydrostatic pressure about 1.7 GPa, the band gap can be closed and then inverted with a critical Dirac point appearing at the Z point.

ACKNOWLEDGMENTS

This work at Ames Laboratory was supported by the U.S. Department of Energy, Office of Science, Basic Energy Sciences, Materials Sciences and Engineering Division. The Ames Laboratory is operated for the U.S. Department of Energy by Iowa State University under Contract No. DE-AC02-07CH11358.

[1] M. Z. Hasan and C. L. Kane, Colloquium: Topological insulators, Rev. Mod. Phys. **82**, 3045 (2010).
[2] X.-L. Qi and S.-C. Zhang, Topological insulators and superconductors, Rev. Mod. Phys. **83**, 1057 (2011).
[3] A. Bansil, H. Lin, and T. Das, Colloquium: Topological band theory, Rev. Mod. Phys. **88**, 021004 (2016).
[4] N. P. Armitage, E. J. Mele, and A. Vishwanath, Weyl and Dirac semimetals in three-dimensional solids, Rev. Mod. Phys. **90**, 015001 (2018).
[5] H. C. Po, A. Vishwanath, and H. Watanabe, Symmetry-based indicators of band topology in the 230 space groups, Nat. Commun. **8**, 50 (2017).
[6] R. J. Slager, A. Mesaros, V. Juricic, and J. Zaanen, The space group classification of topological band-insulators, Nat. Phys. **9**, 98 (2013).
[7] J. Kruthoff, J. de Boer, J. van Wezel, C. L. Kane, and R.-J. Slager, Topological Classification of Crystalline Insulators Through Band Structure Combinatorics, Phys. Rev. X **7**, 041069 (2017).
[8] B. Bradlyn, L. Elcoro, J. Cano, M. G. Vergniory, Z. J. Wang, C. Felser, M. I. Aroyo, and B. A. Bernevig, Topological quantum chemistry, Nature (London) **547**, 298 (2017).
[9] E. Khalaf, H. C. Po, A. Vishwanath, and H. Watanabe, Symmetry Indicators and Anomalous Surface States of Topological Crystalline Insulators, Phys. Rev. X **8**, 031070 (2018).
[10] Z. D. Song, T. T. Zhang, Z. Fang, and C. Fang, Quantitative mappings between symmetry and topology in solids, Nat. Commun. **9**, 3530 (2018).
[11] H. Watanabe, H. C. Po, and A. Vishwanath, Structure and topology of band structures in the 1651 magnetic space groups, Sci. Adv. **4**, eaat8685 (2018).
[12] F. Tang, H. C. Po, A. Vishwanath, and X. G. Wan, Comprehensive search for topological materials using symmetry indicators, Nature (London) **566**, 486 (2019).
[13] T. T. Zhang, Y. Jiang, Z. D. Song, H. Huang, Y. Q. He, Z. Fang, H. M. Weng, and C. Fang, Catalogue of topological electronic materials, Nature (London) **566**, 475 (2019).
[14] M. G. Vergniory, L. Elcoro, C. Felser, N. Regnault, B. A. Bernevig, and Z. J. Wang, A complete catalogue of high-quality topological materials, Nature (London) **566**, 480 (2019).
[15] Y. Xu, L. Elcoro, Z.-D. Song, B. J. Wieder, M. G. Vergniory, N. Regnault, Y. Chen, C. Felser, and B. A. Bernevig, High-throughput calculations of magnetic topological materials, Nature (London) **586**, 702 (2020).

[16] H. M. Weng, X. Dai, and Z. Fang, Transition-Metal Pentatelluride $ZrTe_5$ and $HfTe_5$: A Paradigm for Large-Gap Quantum Spin Hall Insulators, Phys. Rev. X **4**, 011002 (2014).

[17] Q. Li, D. E. Kharzeev, C. Zhang, Y. Huang, I. Pletikosic, A. V. Fedorov, R. D. Zhong, J. A. Schneeloch, G. D. Gu, and T. Valla, Chiral magnetic effect in $ZrTe_5$, Nat. Phys. **12**, 550 (2016).

[18] C. Vaswani, L. L. Wang, D. H. Mudiyanselage, Q. Li, P. M. Lozano, G. D. Gu, D. Cheng, B. Song, L. Luo, R. H. J. Kim, C. Huang, Z. Liu, M. Mootz, I. E. Perakis, Y. Yao, K. M. Ho, and J. Wang, Light-Driven Raman Coherence as a Nonthermal Route to Ultrafast Topology Switching in a Dirac Semimetal, Phys. Rev. X **10**, 021013 (2020).

[19] L. Luo, D. Cheng, B. Song, L.-L. Wang, C. Vaswani, P. M. Lozano, G. Gu, C. Huang, R. H. J. Kim, Z. Liu, J.-M. Park, Y. Yao, K. Ho, I. E. Perakis, Q. Li, and J. Wang, A light-induced phononic symmetry switch and giant dissipationless topological photocurrent in $ZrTe_5$, Nat. Mater. **20**, 329 (2021).

[20] L.-L. Wang, Expansive open Fermi arcs and connectivity changes induced by infrared phonons in $ZrTe_5$, Phys. Rev. B **103**, 075105 (2021).

[21] S. V. Eremeev, G. Landolt, T. V. Menshchikova, B. Slomski, Y. M. Koroteev, Z. S. Aliev, M. B. Babanly, J. Henk, A. Ernst, L. Patthey, A. Eich, A. A. Khajetoorians, J. Hagemeister, O. Pietzsch, J. Wiebe, R. Wiesendanger, P. M. Echenique, S. S. Tsirkin, I. R. Amiraslanov, J. H. Dil, and E. V. Chulkov, Atom-specific spin mapping and buried topological states in a homologous series of topological insulators, Nat. Commun. **3**, 635 (2012).

[22] K. Kuroda, H. Miyahara, M. Ye, S. V. Eremeev, Y. M. Koroteev, E. E. Krasovskii, E. V. Chulkov, S. Hiramoto, C. Moriyoshi, Y. Kuroiwa, K. Miyamoto, T. Okuda, M. Arita, K. Shimada, H. Namatame, M. Taniguchi, Y. Ueda, and A. Kimura, Experimental Verification of $PbBi_2Te_4$ as a 3D Topological Insulator, Phys. Rev. Lett. **108**, 206803 (2012).

[23] M. M. Otrokov, I. I. Klimovskikh, H. Bentmann, D. Estyunin, A. Zeugner, Z. S. Aliev, S. Gaß, A. U. B. Wolter, A. V. Koroleva, A. M. Shikin, M. Blanco-Rey, M. Hoffmann, I. P. Rusinov, A. Y. Vyazovskaya, S. V. Eremeev, Y. M. Koroteev, V. M. Kuznetsov, F. Freyse, J. Sánchez-Barriga, I. R. Amiraslanov, M. B. Babanly, N. T. Mamedov, N. A. Abdullayev, V. N. Zverev, A. Alfonsov, V. Kataev, B. Büchner, E. F. Schwier, S. Kumar, A. Kimura, L. Petaccia, G. Di Santo, R. C. Vidal, S. Schatz, K. Kißner, M. Ünzelmann, C. H. Min, S. Moser, T. R. F. Peixoto, F. Reinert, A. Ernst, P. M. Echenique, A. Isaeva, and E. V. Chulkov, Prediction and observation of an antiferromagnetic topological insulator, Nature (London) **576**, 416 (2019).

[24] D. Zhang, M. Shi, T. Zhu, D. Xing, H. Zhang, and J. Wang, Topological Axion States in the Magnetic Insulator $MnBi_2Te_4$ with the Quantized Magnetoelectric Effect, Phys. Rev. Lett. **122**, 206401 (2019).

[25] P. Swatek, Y. Wu, L.-L. Wang, K. Lee, B. Schrunk, J. Yan, and A. Kaminski, Gapless Dirac surface states in the antiferromagnetic topological insulator $MnBi_2Te_4$, Phys. Rev. B **101**, 161109(R) (2020).

[26] N. H. Jo, L.-L. Wang, R.-J. Slager, J. Yan, Y. Wu, K. Lee, B. Schrunk, A. Vishwanath, and A. Kaminski, Intrinsic axion insulating behavior in antiferromagnetic $MnBi_6Te_{10}$, Phys. Rev. B **102**, 045130 (2020).

[27] Y.-J. Hao, P. Liu, Y. Feng, X.-M. Ma, E. F. Schwier, M. Arita, S. Kumar, C. Hu, R. Lu, M. Zeng, Y. Wang, Z. Hao, H.-Y. Sun, K. Zhang, J. Mei, N. Ni, L. Wu, K. Shimada, C. Chen, Q. Liu, and C. Liu, Gapless Surface Dirac Cone in Antiferromagnetic Topological Insulator $MnBi_2Te_4$, Phys. Rev. X **9**, 041038 (2019).

[28] Y. J. Chen, L. X. Xu, J. H. Li, Y. W. Li, H. Y. Wang, C. F. Zhang, H. Li, Y. Wu, A. J. Liang, C. Chen, S. W. Jung, C. Cacho, Y. H. Mao, S. Liu, M. X. Wang, Y. F. Guo, Y. Xu, Z. K. Liu, L. X. Yang, and Y. L. Chen, Topological Electronic Structure and its Temperature Evolution in Antiferromagnetic Topological Insulator $MnBi_2Te_4$, Phys. Rev. X **9**, 041040 (2019).

[29] H. Li, S.-Y. Gao, S.-F. Duan, Y.-F. Xu, K.-J. Zhu, S.-J. Tian, J.-C. Gao, W.-H. Fan, Z.-C. Rao, J.-R. Huang, J.-J. Li, D.-Y. Yan, Z.-T. Liu, W.-L. Liu, Y.-B. Huang, Y.-L. Li, Y. Liu, G.-B. Zhang, P. Zhang, T. Kondo, S. Shin, H.-C. Lei, Y.-G. Shi, W.-T. Zhang, H.-M. Weng, T. Qian, and H. Ding, Dirac Surface States in Intrinsic Magnetic Topological Insulators $EuSn_2As_2$ and $MnBi_{2n}Te_{3n+1}$, Phys. Rev. X **9**, 041039 (2019).

[30] Y. Deng, Y. Yu, Z. Shi Meng, Z. Guo, Z. Xu, J. Wang, H. Chen Xian, and Y. Zhang, Quantum anomalous Hall effect in intrinsic magnetic topological insulator $MnBi_2Te_4$, Science **367**, 895 (2020).

[31] C. Liu, Y. Wang, H. Li, Y. Wu, Y. Li, J. Li, K. He, Y. Xu, J. Zhang, and Y. Wang, Robust axion insulator and Chern insulator phases in a two-dimensional antiferromagnetic topological insulator, Nat. Mater. **19**, 522 (2020).

[32] T. Zhu, A. J. Bishop, T. Zhou, M. Zhu, D. J. O'Hara, A. A. Baker, S. Cheng, R. C. Walko, J. J. Repicky, T. Liu, J. A. Gupta, C. M. Jozwiak, E. Rotenberg, J. Hwang, I. Žutić, and R. K. Kawakami, Synthesis, magnetic properties, and electronic structure of magnetic topological insulator $MnBi_2Se_4$, Nano Lett. **21**, 5083 (2021).

[33] Y. Hattori, Y. Tokumoto, K. Kimoto, and K. Edagawa, Evidences of inner Se ordering in topological insulator $PbBi_2Te_4$-$PbBi_2Se_4$-$PbSb_2Se_4$ solid solutions, Sci. Rep. **10**, 7957 (2020).

[34] A. A. Sher, I. N. Odin, and A. V. Novoselova, Interaction in the system Sn-Bi-Se, Inorg. Mater. **14**, 993 (1978).

[35] K. A. Agaev and S. A. Semiletov, Electron-diffraction study of the structure of $PbBi_2Se_4$, Sov. Phys. Crystallogr. **13**, 201 (1968).

[36] A. D. Becke and E. R. Johnson, A simple effective potential for exchange, J. Chem. Phys. **124**, 221101 (2006).

[37] P. Hohenberg and W. Kohn, Inhomogeneous electron gas, Phys. Rev. **136**, B864 (1964).

[38] W. Kohn and L. J. Sham, Self-consistent equations including exchange and correlation effects, Phys. Rev. **140**, A1133 (1965).

[39] G. Kresse and J. Furthmuller, Efficiency of ab-initio total energy calculations for metals and semiconductors using a plane-wave basis set, Comput. Mater. Sci. **6**, 15 (1996).

[40] G. Kresse and J. Furthmuller, Efficient iterative schemes for ab initio total-energy calculations using a plane-wave basis set, Phys. Rev. B **54**, 11169 (1996).

[41] J. P. Perdew, A. Ruzsinszky, G. I. Csonka, O. A. Vydrov, G. E. Scuseria, L. A. Constantin, X. Zhou, and K. Burke, Restoring the Density-Gradient Expansion for Exchange in Solids and Surfaces, Phys. Rev. Lett. **100**, 136406 (2008).

[42] J. Klimes, D. R. Bowler, and A. Michaelides, van der Waals density functionals applied to solids, Phys. Rev. B **83**, 195131 (2011).

[43] S. Grimme, Semiempirical GGA-type density functional constructed with a long-range dispersion correction, J. Comput. Chem. **27**, 1787 (2006).

[44] S. Grimme, J. Antony, S. Ehrlich, and H. Krieg, A consistent and accurate ab initio parametrization of density functional dispersion correction (DFT-D) for the 94 elements H-Pu, J. Chem. Phys. **132**, 154104 (2010).

[45] S. Grimme, S. Ehrlich, and L. Goerigk, Effect of the damping function in dispersion corrected density functional theory, J. Comput. Chem. **32**, 1456 (2011).

[46] H. J. Monkhorst and J. D. Pack, Special points for Brillouin-zone integrations, Phys. Rev. B **13**, 5188 (1976).

[47] N. Marzari and D. Vanderbilt, Maximally localized generalized Wannier functions for composite energy bands, Phys. Rev. B **56**, 12847 (1997).

[48] I. Souza, N. Marzari, and D. Vanderbilt, Maximally localized Wannier functions for entangled energy bands, Phys. Rev. B **65**, 035109 (2001).

[49] M. P. L. Sancho, J. M. L. Sancho, and J. Rubio, Quick iterative scheme for the calculation of transfer matrices: Application to Mo(100), J. Phys. F: Met. Phys. **14**, 1205 (1984).

[50] M. P. L. Sancho, J. M. L. Sancho, and J. Rubio, Highly convergent schemes for the calculation of bulk and surface Green-functions, J. Phys. F: Met. Phys. **15**, 851 (1985).

[51] Q. Wu, S. Zhang, H.-F. Song, M. Troyer, and A. A. Soluyanov, WannierTools: An open-source software package for novel topological materials, Comput. Phys. Commun. **224**, 405 (2018).

[52] H. Chen, G. Hautier, and G. Ceder, Synthesis, computed stability, and crystal structure of a new family of inorganic compounds: Carbonophosphates, J. Am. Chem. Soc. **134**, 19619 (2012).

[53] J. Qiao, X. Kong, Z.-X. Hu, F. Yang, and W. Ji, High-mobility transport anisotropy and linear dichroism in few-layer black phosphorus, Nat. Commun. **5**, 4475 (2014).

[54] K. Choudhary, Q. Zhang, A. C. E. Reid, S. Chowdhury, N. Van Nguyen, Z. Trautt, M. W. Newrock, F. Y. Congo, and F. Tavazza, Computational screening of high-performance optoelectronic materials using OptB88vdW and TB-mBJ formalisms, Sci. Data **5**, 180082 (2018).

[55] M. Nurmamat, K. Okamoto, S. Zhu, T. V. Menshchikova, I. P. Rusinov, V. O. Korostelev, K. Miyamoto, T. Okuda, T. Miyashita, X. Wang, Y. Ishida, K. Sumida, E. F. Schwier, M. Ye, Z. S. Aliev, M. B. Babanly, I. R. Amiraslanov, E. V. Chulkov, K. A. Kokh, O. E. Tereshchenko, K. Shimada, S. Shin, and A. Kimura, Topologically nontrivial phase-change compound $GeSb_2Te_4$, ACS Nano **14**, 9059 (2020).

[56] M. Neupane, S. Y. Xu, L. A. Wray, A. Petersen, R. Shankar, N. Alidoust, C. Liu, A. Fedorov, H. Ji, J. M. Allred, Y. S. Hor, T. R. Chang, H. T. Jeng, H. Lin, A. Bansil, R. J. Cava, and M. Z. Hasan, Topological surface states and Dirac point tuning in ternary topological insulators, Phys. Rev. B **85**, 235406 (2012).

[57] M. Arita, H. Sato, K. Shimada, H. Namatame, M. Taniguchi, M. Sasaki, M. Kitaura, A. Ohnishi, and H.-J. Kim, Angle resolved photoemission study of $GeBi_2Te_4$, JPS Conf. Proc. **1**, 012017 (2014).

[58] D. Niesner, S. Otto, V. Hermann, T. Fauster, T. V. Menshchikova, S. V. Eremeev, Z. S. Aliev, I. R. Amiraslanov, M. B. Babanly, P. M. Echenique, and E. V. Chulkov, Bulk and surface electron dynamics in a *p*-type topological insulator $SnSb_2Te_4$, Phys. Rev. B **89**, 081404(R) (2014).

[59] J. A. Sans, R. Vilaplana, E. L. da Silva, C. Popescu, V. P. Cuenca-Gotor, A. Andrada-Chacón, J. Sánchez-Benitez, O. Gomis, A. L. J. Pereira, P. Rodríguez-Hernández, A. Muñoz, D. Daisenberger, B. García-Domene, A. Segura, D. Errandonea, R. S. Kumar, O. Oeckler, P. Urban, J. Contreras-García, and F. J. Manjón, Characterization and decomposition of the natural van der Waals $SnSb_2Te_4$ under compression, Inorg. Chem. **59**, 9900 (2020).

[60] L. Fu and C. L. Kane, Topological insulators with inversion symmetry, Phys. Rev. B **76**, 045302 (2007).

[61] J. M. DeStefano and L.-L. Wang, Pressure effect on band inversion in $AECd_2As_2$ (AE = Ca, Sr, Ba), Phys. Rev. B **103**, 115207 (2021).